

# Thickness- and Twist-Angle-Dependent Interlayer Excitons in Metal Monochalcogenide Heterostructures

Wenkai Zheng, Li Xiang, Felipe A. de Quesada, Mathias Augustin, Zhengguang Lu, Matthew Wilson, Aditya Sood, Fengcheng Wu, Dmitry Shcherbakov, Shahriar Memaran, Ryan E. Baumbach, Gregory T. McCandless, Julia Y. Chan, Song Liu, James H. Edgar, Chun Ning Lau, Chun Hung Lui, Elton J. G. Santos, Aaron Lindenberg, Dmitry Smirnov, and Luis Balicas\*

Cite This: <https://doi.org/10.1021/acsnano.2c07394>

Read Online

ACCESS |

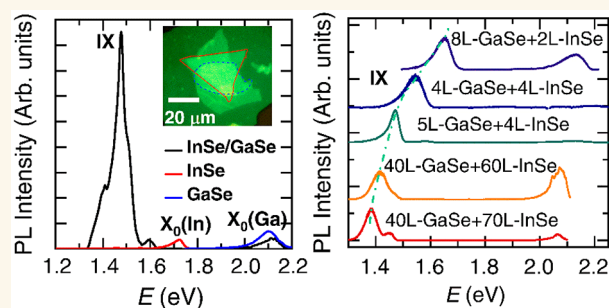
Metrics & More

Article Recommendations

Supporting Information

**ABSTRACT:** Interlayer excitons, or bound electron–hole pairs whose constituent quasiparticles are located in distinct stacked semiconducting layers, are being intensively studied in heterobilayers of two-dimensional semiconductors. They owe their existence to an intrinsic type-II band alignment between both layers that convert these into p–n junctions. Here, we unveil a pronounced interlayer exciton (IX) in heterobilayers of metal monochalcogenides, namely,  $\gamma$ -InSe on  $\epsilon$ -GaSe, whose pronounced emission is adjustable just by varying their thicknesses given their number of layers dependent direct band gaps. Time-dependent photoluminescence spectroscopy unveils considerably longer interlayer exciton lifetimes with respect to intralayer ones, thus confirming their nature. The linear Stark effect yields a bound electron–hole pair whose separation  $d$  is just  $(3.6 \pm 0.1)$  Å with  $d$  being very close to  $d_{\text{Se}} = 3.4$  Å which is the calculated interfacial Se separation. The envelope of IX is twist-angle-dependent and describable by superimposed emissions that are nearly equally spaced in energy, as if quantized due to localization induced by the small moiré periodicity. These heterostacks are characterized by extremely flat interfacial valence bands making them prime candidates for the observation of magnetism or other correlated electronic phases upon carrier doping.

**KEYWORDS:** photoluminescence, interlayer excitons, metal monochalcogenides, heterostructures, Stark effect, moiré potential



Long-lived excitons, or bound electron–hole pairs created by promoting electrons from the valence to the conduction band, have been proposed as possible building blocks for coherent quantum many-body condensates<sup>1–3</sup> or even as quantum information carriers.<sup>4,5</sup> In conventional semiconductors, the exciton lifetime can be increased by building double–quantum wells, where spatially separated electrons and holes become bound to form so-called interlayer excitons (IXs).<sup>6–12</sup> Strongly bound IXs can also be formed by stacking, for instance, two single unit cells of transition metal dichalcogenides (TMDs) forming a van der Waals (vdW) heterostructure. Such heterostructures (e.g., MoSe<sub>2</sub> on WSe<sub>2</sub>, or MoS<sub>2</sub> on WS<sub>2</sub>, etc.) display ultrafast charge transfer,<sup>13</sup> IXs with binding energies as large as  $\sim 150$  meV,<sup>14</sup> and an ability to diffuse over large distances.<sup>15</sup> Furthermore, their tight binding and small Bohr radius can potentially lead to quantum degeneracy between such composite bosons leading to exciton condensation at substantially elevated temperatures

when compared, for instance, with those required for conventional Bose–Einstein condensation in cold atoms.<sup>2</sup>

In TMD monolayers the spatial separation between bound charge carriers in distinct layers yields distinct properties to IXs when compared to those of the intralayer excitons ( $X_0$ ), due to the reduced overlap between electron and hole wave functions. In quantum wells the lifetime of their indirect IX greatly exceeds that of the direct excitons,<sup>16</sup> allowing them to thermalize with the lattice prior to recombination. Furthermore, the electron–hole separation results in a permanent

Received: July 25, 2022

Accepted: October 12, 2022

electric dipole moment, which creates repulsive dipole–dipole interactions.<sup>17</sup> In stacked TMD monolayers, the IXs possess properties that result from the vdW coupling between layers, enhanced Coulomb interactions at the 2D limit, in combination with the intrinsic valley properties of the constituent layers (e.g., locked electron spin and layer indices).<sup>18</sup> In effect, a lattice mismatch between heterobilayers, or a small twist angle between homobilayers, leads to a long-range periodicity or moiré pattern that affects their overall optical response and therefore the properties of the excitons in 2D vdW semiconducting layers.<sup>19–25</sup>

Scanning tunneling microscopy (STM) performed on MoS<sub>2</sub>/WSe<sub>2</sub> heterobilayers,<sup>26,27</sup> reveals a periodically modulated local band gap within the moiré unit cell. This forms a two-dimensional electronic superlattice whose electronic wave functions are spatially localized within the potential minima of the individual moiré unit cells. Moiré quantum systems display electronic, optical, and topological properties that are tunable with an exquisite level of control.<sup>19,21–25,28–33</sup> However, to date the moiré physics has been constrained by two factors: (i) the dimensionality, defined by the stacking of monolayers,<sup>28</sup> and (ii) the twist angle  $\phi$ , which unveils superconductivity,<sup>30</sup> orbital magnetism,<sup>31</sup> and correlated insulator states<sup>25,29</sup> only at precise values of  $\phi$ . The moiré potential in WSe<sub>2</sub>/WS<sub>2</sub> heterostructures is much stronger than the exciton kinetic energy, and generates multiple flat excitonic minibands that strongly alter the intralayer exciton emissions of WSe<sub>2</sub>.<sup>21</sup> TMD monolayers have a direct band gap located at the degenerate  $K$ ,  $K'$  points at the corners of their unfolded Brillouin zone. However, efficient light emission from IX recombination requires bound electron–holes to emerge from almost the same momentum in reciprocal space. In twisted TMD heterobilayers, a pronounced IX emission is observed only for twist angles approaching either 0 or 60° due to a momentum mismatch between the minimum in energy of the conduction band and the valence band maximum at larger twist angles. This mismatch suppresses emissions at intermediate angles<sup>34</sup> where umklapp recombination processes contribute to a weak emission.<sup>23</sup>

In this work, we introduce another platform to explore the physics of the interlayer excitons and possibly the role of the moiré potential on the optoelectronic response of layered semiconductors: stacked semiconducting metal-monochalcogenides (MMCs) or  $\gamma$ -InSe/ $\epsilon$ -GaSe heterostructures fabricated under inert atmosphere (see the “Methods” section). Similar to TMDs, the band gaps of both  $\epsilon$ -GaSe and  $\gamma$ -InSe progressively increase as the number of layers is reduced<sup>35</sup> albeit evolving from direct to indirect. Bulk  $\gamma$ -InSe displays a direct band gap of 1.25 eV but transitions to a 2.9 eV indirect one in the single layer limit,<sup>36</sup> while the 2 eV band gap of bulk  $\epsilon$ -GaSe increases up to  $\sim$ 2.4 eV in bilayers<sup>35</sup> (Figure 1). This behavior implies that the relative type-II band alignment<sup>37</sup> between  $\gamma$ -InSe and  $\epsilon$ -GaSe can be modified simply by stacking layers having distinct thicknesses. This provides an additional level of tunability for the energy of the interlayer exciton in  $\gamma$ -InSe/ $\epsilon$ -GaSe heterostructures and contrasts with the TMDs that display a direct band gap only at the monolayer limit.<sup>38</sup> In addition, the direct band gap of both compounds, except perhaps for their bilayers and monolayers, is at the  $\Gamma$ -point of their Brillouin zone.<sup>35</sup> This absence of momentum mismatch between electrons and holes in adjacent layers, regardless of their twist angle, would represent an advantage with respect to TMDs for studying interlayer excitonic

emissions as well as the possible effect of the moiré potential on them. In MMCs, band structure calculations indicate that optically induced interlayer electronic transitions would always be direct in  $k$ -space (except for their monolayers).<sup>35,39</sup> The fact that InSe/GaSe heterostructures form type-II band alignments despite variations in the thicknesses of the constituent layers, was already discussed in several reports.<sup>35,37,40,41</sup>

Here, we show through photoluminescence measurements that InSe/GaSe heterostructures encapsulated among  $h$ -BN layers display a very pronounced and multicomponent interlayer exciton emission whose energy can be tuned by varying the thickness of the constituent layers. The lifetime of the interlayer exciton is considerably longer than those of the constituent layers, as observed in TMDs. Under an electric field, the associated Stark effect is dominated by the linear term yielding a dipole separation of just ( $3.6 \pm 0.1$ ) Å. When the IX emission is decomposed into its components, the higher energy superimposed emissions also display the second-order Stark effect, with both observations being akin to those from hydrogen atoms, suggesting relatively isotropic wave functions for IXs. Finally, we show that the multicomponent IX emissions display similarities with moiré exciton behavior in TMDs, namely, twist-angle-dependent energy quantization that is reproducible in every location across the interface. This would suggest small radii for the interlayer excitons in metal monochalcogenides when compared to those of TMDs.<sup>42</sup>

## RESULTS AND DISCUSSION

**Thickness-Dependent Photoluminescence in  $\gamma$ -InSe/ $\epsilon$ -GaSe Heterostructures.** The heterostructures were fabricated from exfoliated high quality bulk single-crystals of  $\gamma$ -InSe and  $\epsilon$ -GaSe. Crystal synthesis protocols are described in the “Methods” section. Our  $\gamma$ -InSe crystals yield quantum Hall effect and mobilities exceeding 4000 cm<sup>2</sup>/(V s).<sup>43</sup> Single-crystal X-ray diffraction (Figure S1) reveals no stacking mosaicity in the  $\epsilon$ -GaSe. A simple schematic of our heterostructures (Figure 1a) illustrates that the individual layers are not grounded during the measurements and therefore cannot be doped upon gating. Few-layered graphite was transferred on top of the stack to act as the top electrical gate. InSe and GaSe share a planar hexagonal structure but with distinct lattice constants of  $a_0 = 4.08(2)$  Å and  $a = 3.7557(3)$  Å, respectively. This marked difference is sufficient to generate a moiré modulation even when both layers are perfectly aligned. For twisted layers, the moiré periodicity  $\lambda$  as a function of twist-angle  $\phi$  would range from a mere  $\lambda \sim 5$  nm ( $\phi = 0^\circ$ ) to just 0.7 nm ( $\phi = 30^\circ$ ), see ref.<sup>44</sup> If the Bohr radius of IX was smaller than  $\lambda$ , IX would sense the moiré potential and become confined by it. In fact, the separation and confinement of the bound electron–hole pairs in spatially separated layers is expected to make IXs particularly susceptible to the moiré potential at the interface.<sup>21</sup>

The type-II band alignment between both compounds, leading to a near direct band gap at the  $\Gamma$ -point, is supported by band structure calculations for monolayers (Figure 1b) as well as few-layered crystals having a similar number of layers ( $L$ , Figure S2). To understand the interfacial electronic structure, we performed van der Waals (vdW) corrected ab initio simulations finding a large interfacial charge density involving the Se atoms of both materials; they are separated by just 3.4 Å (Figure 1c). This proximity between interfacial Se–Se atoms induces a strong interlayer coupling of near-covalent character that maximizes the role of the moiré potential or

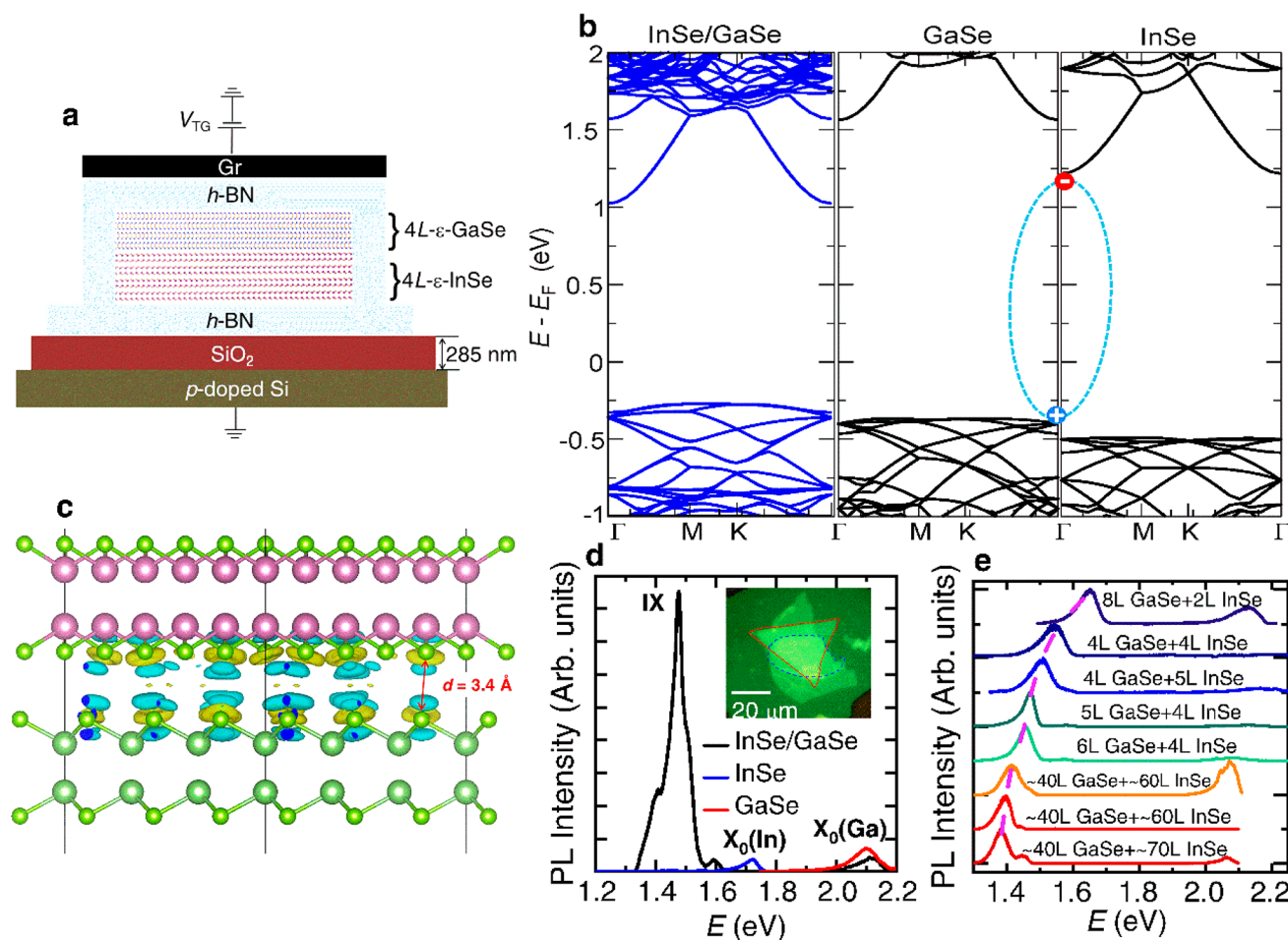


**Figure 1.** Photoluminescence spectra from  $\gamma$ -InSe/ $\epsilon$ -GaSe heterostructures displaying interlayer exciton emission. (a) Sketch of a typical heterostructure based on  $n$ (Ga) $L$ - $\epsilon$ -GaSe on  $n$ (In) $L$ - $\gamma$ -InSe encapsulated among  $h$ -BN layers (clear blue) with the entire stack transferred onto  $\text{SiO}_2$  (granate). A thin layer of graphite (Gr) (thickness  $\sim 100$  nm) was transferred to the top of the stack to act as the top electrical gate with  $h$ -BN acting as the dielectric layer. Notice that the individual layers are not connected to the electrical ground. Therefore, the application of an electric field via either the top or the bottom gates cannot charge dope the constituent layers or the interface. (b) Left to right: band structures of a stack composed of monolayer (1L)  $\epsilon$ -GaSe and 1L- $\gamma$ -InSe, 1L- $\epsilon$ -GaSe (center), and 1L- $\gamma$ -InSe (right) within the reduced moiré Brillouin zone where the twist angle is  $\phi = 0^\circ$ . Here, the position of the conduction and valence bands of 1L- $\epsilon$ -GaSe (center) relative to those of 1L- $\gamma$ -InSe (right) illustrates their type-II band alignment. The folded and quite flat valence band of 1L- $\epsilon$ -GaSe within the moiré Brillouin zone, allows the formation of an interlayer exciton with the electron promoted to the conduction band minimum of 1L- $\gamma$ -GaSe located at the  $\Gamma$ -point. This lack of momentum mismatch between maximum and minimum is favorable to the creation of interlayer excitons (blue and red dots encircled by dotted line depict the interlayer exciton at  $\Gamma$ ), regardless of the twist angle. (c) Difference in charge density ( $2 \times 10^5$  eV/Å<sup>3</sup>) at the InSe/GaSe interface calculated through vdW-corrected *ab initio* simulation methods. The charge density is confined mainly at the interface and involves the Se atoms from both materials, which are separated by 3.4 Å. The small Se–Se distance at the interface (3.4 Å) is close to the lengths of the chemical bonds in In–Se (2.60 Å) and Ga–Se (2.50 Å). This proximity of the Se–Se atoms at the interface induces a covalent character altogether with the vdW interactions. In the plot, big purple (green) atoms depict Ga (In), and small green atoms correspond to Se. In Figures S3–S5, we provide the calculated electronic charge distribution, the electrical potential, and electric field as a function of the interlayer distance  $z$ , indicating that these heterostructures form PN-junctions. (d) Measured PL spectra from a  $n$ (In) = 4L InSe layer (blue line), a  $n$ (Ga) = 5L- $\epsilon$ -GaSe (red line), and from their interface (black line). The interfacial exciton IX peaks at a lower energy with respect to the intralayer excitons  $X_0$ (Ga) and  $X_0$ (In) of the individual constituent layers, thus indicating that IX originates from an interlayer transition. Notice its multicomponent nature. Inset: optical microscopy image of the  $h$ -BN encapsulated 4L- $\epsilon$ -GaSe/5L- $\gamma$ -InSe heterostructure where the GaSe flake is delineated by a solid red line with the InSe one delineated by a blue dashed line. (e) Photoluminescence (PL) spectra for several  $n$ (Ga) $L$ - $\epsilon$ -GaSe/ $n$ (In) $L$ - $\gamma$ -InSe heterostructures, with the number of layers ( $L$ ) varying between  $n$ (Ga) = 4 and 40, and  $n$ (In) varying from  $\sim 2$  to  $\sim 70$ , measured at  $T = 5$  K. In this panel all curves are offset for clarity. Owing to the type-II band alignment between both compounds, the interlayer exciton emission (or IX, indicated by the dotted line) is located between  $\sim 1.39$  and 1.65 eV as the thicknesses of the constituent layers decrease. In contrast, the intralayer exciton emission for both InSe and GaSe become strongly quenched in the junction area.

leads to deeper moiré potential wells relative to conventional vdW coupled layers. The calculated electronic charge densities (Figure S3) and associated potential difference (Figure S4) lead to a pronounced interfacial electric field (Figure S5). Our calculations are supported by previous scanning photoelectron

microscopy measurements in  $\gamma$ -InSe/ $\epsilon$ -GaSe heterostructures that reveal a charge dipole at the interface, with the conduction band offsets suggesting that charge carriers are able to overcome the built-in potential to meet at the interface and form an interlayer exciton.<sup>40</sup>

To evaluate the optical response of these interfaces we collected micro-PL spectra from several  $\gamma$ -InSe/ $\epsilon$ -GaSe heterostructures whose constituent layers vary widely in their thicknesses. The samples were kept at  $T = 5$  K and photoexcited with a continuous-wave  $\nu = 514$  nm laser ( $\nu$  is the wavelength) focused through an objective (of numerical aperture NA = 0.65) to a spot size of  $\sim 2$   $\mu\text{m}$ . For instance, we collected photoluminescence (PL) spectra from a 4L- $\gamma$ -InSe flake on 5L- $\epsilon$ -GaSe (Figure 1d) revealing that the intensity of the IX emission from the interfacial area is considerably more pronounced than those of the intralayer  $X_0(\text{In})$  and  $X_0(\text{Ga})$  emissions collected outside of the interface, despite their direct band gap. In addition, the intensity of  $X_0(\text{In})$  collected in the interfacial area becomes nearly completely suppressed. A similar quenching occurs in TMDs and is attributed to ultrafast interlayer charge transfer.<sup>13,21,23</sup> This quenching is observed in nearly all measured heterostructures, with thicknesses in the ranges of  $n(\text{In}) \cong 2\text{L}$  to  $\cong 72\text{L}$  for  $\gamma$ -InSe and  $n(\text{Ga}) \cong 4\text{L}$  to  $\cong 38\text{L}$  for  $\epsilon$ -GaSe (Figure 1e).

The IX emission observed at 1.38 eV in thick constituent layers increases up to 1.65 eV (indicated by the dotted line) as their thicknesses decrease or as their band gap increases. We note the relative agreement between these values and the calculated energy separation between valence and conduction bands (Figures 1b and S2). As previously mentioned, Figures S6–S8 display a comparison between emissions from the interfacial area and those from the intralayer excitons associated exclusively with the  $\gamma$ -InSe and  $\epsilon$ -GaSe areas located beyond the interface. The important point is that this pronounced IX peak does not coincide with either  $X_0(\text{In})$  or  $X_0(\text{Ga})$ , albeit for thick layers it partially overlaps with  $X_0(\text{In})$ . Therefore, it ought to correspond to emissions from interlayer excitons (here, the term “interlayer” means distributed across both materials). From the overall data collected by us, we observe that to first approximation the energy of the interlayer exciton  $E(\text{IX})$  follows a power law dependence on both  $n(\text{In})$  and  $n(\text{Ga})$  (i.e.,  $E(\text{IX}) \propto [n(\text{Ga}, \text{In})]^\alpha$ , with exponents  $\alpha(\text{In}) = -(35 \pm 9)$  and  $\alpha(\text{Ga}) = -(30 \pm 4)$ ). This leads to the expression  $E(\text{IX}) = a[n(\text{Ga})]^\alpha(\text{Ga}) + b[n(\text{In})]^\alpha(\text{In})$ , with coefficients  $a \cong 2.52$  eV and  $b = -0.86$  eV, providing a rough estimate for the value of  $E(\text{IX})$  as a function of either number of layers.

In Figure S7 we have replotted the PL spectra displayed in Figure 1e, fitting them to a set of three Gaussian functions that allow us to decompose the IX emissions. Figure S7 also allows a closer inspection of the precise position in energy of the IX emissions from each heterostructure. As seen, most IX emissions can be fit well to just three Gaussians whose separation in energy is heterostructure-dependent. For several heterostructures we also detect the intralayer exciton  $X_0(\text{In})$  in the vicinity of IX. The important observations are as follows: (i) The separation in energy  $\Delta E$  between all three IX emission is nearly constant, as is the case for the few heterostructures discussed below, (ii) but the separation in energy between the highest IX emission and the one from  $X_0(\text{In})$  is considerably larger with  $X_0(\text{In})$  showing a much lower amplitude, which allows us to differentiate them. As discussed below and in the Supporting Information, the emissions yielding IX do not match the  $X_0(\text{In})$  ones measured at low temperatures for bulk  $\gamma$ -InSe implying that they have a distinct origin.

As seen in Figures S6–S8, both the  $X_0(\text{In})$  and  $X_0(\text{Ga})$  emissions become strongly quenched in the junction area, but this quenching is particularly pronounced for samples

characterized by  $\phi < 20^\circ$ . This implies that  $\phi$  affects the charge transfer across the interface with this transfer becoming particularly fast or efficient at smaller values of  $\phi$ . Throughout this text, the values of  $\phi$  were determined through second harmonic generation (see, Figures S9–S14).

**Evaluation of Exciton Lifetimes through Time-Dependent PL.** In TMDs, the IX emissions display considerably longer lifetimes relative to the intralayer ones,<sup>14,22,45–48</sup> with their lifetimes being modulated by factors like the incident illumination power<sup>49</sup> or the twist angle between heterobilayers<sup>50</sup> (i.e., as the direct optical transition (for  $\phi = 0^\circ$ ) at the  $K$ -point becomes indirect upon increasing  $\phi$  and leading to excitons with a center of mass momentum).<sup>50</sup> The measured IX lifetimes  $\tau$  varies widely,<sup>14,22,45–51</sup> from values in the range of  $\tau \cong 10^{-1}$  to  $\cong 10^2$  ns. The reason for this variability in the values of  $\tau$  remains unclear, although the superposition of an additional indirect optical transition when  $\phi > 0^\circ$  or the scattering between bright and dark excitons may explain heterostructure-dependent values for  $\tau$ .<sup>50,52</sup> These same factors might also explain the characteristic two exponential decaying times of the photoluminescent response.<sup>46,50</sup>

To further characterize the nature of the IX emission, we have also conducted time-dependent photoluminescence measurements (Figure 2) in a 4L- $\gamma$ -InSe/4L- $\epsilon$ -GaSe heterostructure that is characterized by  $\phi = (9.4 \pm 0.6)^\circ$  (Figure S10). This heterostructure was chosen because it displays clear IX,  $X_0(\text{In})$ , and  $X_0(\text{Ga})$  emissions at 1.52,  $\sim 1.7$ , and  $\sim 2.12$  eV, respectively (Figure 2a). Each emission can be well adjusted to two exponential decays once the instrumental response function is subtracted from the experimentally determined time-dependent photoluminescent signal (Figure 2b). These fits yield values  $\tau_1$  for the shortest decay time of 0.0513, 0.0632, and 0.2808 ns for  $X_0(\text{Ga})$ ,  $X_0(\text{In})$ , and IX, respectively. And  $\tau_2$ , or longer decay times of 2.2030, 0.9739, and 2.7546 ns for  $X_0(\text{Ga})$ ,  $X_0(\text{In})$ , and IX, respectively. These values are comparable or shorter than the exciton lifetimes reported for TMDs.<sup>14,22,45–51</sup> Most importantly, both lifetimes extracted for IX are considerably longer than those associated with the intralayer excitons, as previously reported for TMDs, thus supporting our identification of IX as an interlayer exciton whose emission energy is layer thickness-dependent. We also evaluated the  $\tau_1$  and  $\tau_2$  lifetimes associated with the IX emissions extracted from thicker heterostructures characterized by  $\phi \cong 30$  and  $40^\circ$ , obtaining respectively,  $\tau_1 = 0.1522$  and  $0.1275$  ns or  $\tau_2 = 1.9396$  and  $2.2673$  ns. Hence, larger twist angles would seem to affect  $\tau_1$  considerably in contrast to  $\tau_2$ . A considerable increase in exciton relaxation times as a function of twist angle has already been reported for TMDs.<sup>50</sup> However, to describe the exciton decay times in MMCs, one would have to understand their ground and excited excitonic states, how these couple to acoustic and optical phonons, and how this coupling might be affected by the twist angle. Prior to this, a systematic study in multiple samples will have to be performed to clarify if the differences in  $\tau_1$  are indeed twist-angle- or sample-dependent.

**Stark Effect.** The envelope of IX at any given location should be controllable through the application of an electric field given that interlayer excitons possess an out-of-plane electric dipole moment that is manipulable via an out-of-plane electric field<sup>49</sup> or the Stark effect. For example, the IX emissions from a heterostructure composed of 5L- $\epsilon$ -GaSe on 4L- $\gamma$ -InSe, fit to a minimum set of three Lorentz functions, are

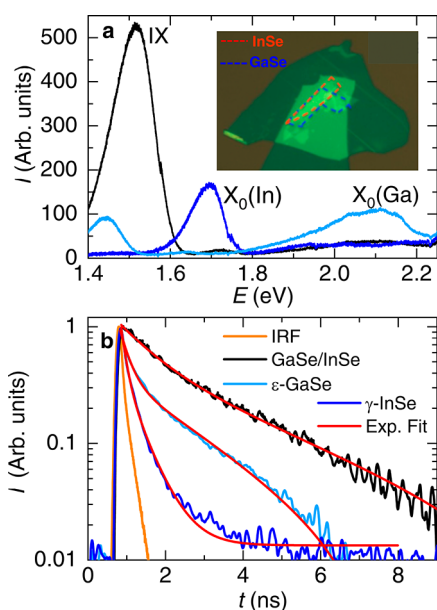


**Figure 2.** Interlayer and intralayer exciton lifetimes. (a) Photoluminescence spectra from a nonannealed 4- $\gamma$ -InSe/4L- $\epsilon$ -GaSe heterostructure (see, Figure S10). Black trace corresponds to the PL spectrum from the junction area, revealing emission peaks at  $\sim 1.52$  and  $\sim 1.7$  eV as well as a broad peak centered at  $\sim 2.12$  eV. Blue trace corresponds to emission from a region of the  $\gamma$ -InSe layer that does not overlap the  $\epsilon$ -GaSe one, indicating that the peak at  $\approx 1.7$  eV corresponds to the intralayer exciton  $X_0(\text{In})$  of  $\gamma$ -InSe. Clear blue trace depicts the emission from the  $\epsilon$ -GaSe layer not in contact with  $\gamma$ -InSe, indicating that the peak at  $2.12$  eV corresponds to the intralayer  $X_0(\text{Ga})$  emission. Therefore, the tall peak at  $1.52$  eV, ought to correspond to the interlayer IX emission. Inset: micrograph of the heterostructure where the boundaries of the  $\gamma$ -InSe and  $\epsilon$ -GaSe crystals are indicated by red and blue dashed lines, respectively. (b) Measurements of the exciton lifetimes through time-dependent photoemission spectroscopy. Here, blue, light blue, and black traces correspond to  $X_0(\text{In})$ ,  $X_0(\text{Ga})$ , and IX respectively. The orange line corresponds to the time-dependent instrument response function (IRF) of the setup used for the measurements. Red lines are fits to two exponential decays, illustrating the existence of two lifetimes. As clearly seen, IX has considerably longer lifetimes with respect to both  $X_0(\text{In})$  and  $X_0(\text{Ga})$ . The actual values of the lifetimes are obtained by deconvoluting the IRF from the experimental time-dependent photoluminescent signal. The goodness of these fits  $R^2$  are 0.99875, 0.99732, and 0.99682 for IX,  $X_0(\text{Ga})$ , and  $X_0(\text{In})$ , respectively.

blue-shifted by approximately 25 meV as the top gate voltage  $V_{\text{TG}}$  (Figure 3a–c) is swept from  $-28$  to  $28$  V. The stark Hamiltonian,  $H_{\text{Stark}} = \mu E$ , describes the coupling between the electric field  $E$  and the exciton electric dipole moment  $\mu = ed$  oriented across the heterostructure ( $d$  is the electron–hole separation). The linear Stark effect is expected in our case, given the lack of inversion symmetry at the interface and the orientation of the dipole moments. Applying an  $E$  antiparallel to  $\mu$  affects the overlap between electron and hole wave functions and therefore the PL emission (as seen in Figure 3b). Similar behavior was reported for twisted TMD heterobilayers,<sup>53</sup> although it was found to be nonlinear and far more pronounced in TMD homobilayers.<sup>54</sup> A linear fit between the electric field applied across the heterostructure  $E_h$  and the energy of the lowest energy emission (centered at  $\sim 1.42$  eV at  $V_{\text{TG}} = 0$  V) yields  $d = (3.6 \pm 0.1)$  Å. This value is close to our

DFT-calculated separation between adjacent interfacial Se atoms ( $3.4$  Å, Figure 1c), thus experimentally confirming our prediction of charge accumulation in the vicinity of the Se atoms. The higher energy IX emissions display a mild nonlinear dependence on  $E_h$  (Figure 3c) that is well-captured by a negative  $E^2$  term associated with the second-order Stark effect. Note that a linear response on electric field for the lower energy emissions, with higher energy ones revealing the superposition of a quadratic term, is precisely the behavior of the hydrogen atom where the electrical polarizability of its atomic orbitals was empirically determined to be proportional to  $n$  the principal quantum number.<sup>55</sup>

The linear dependence on  $E_h$  for IX contrasts markedly with the one displayed by the intralayer exciton emission of 5L- $\gamma$ -InSe (Figure 3d) which displays a mirror symmetric, purely quadratic response with respect to  $E_h = 0$  V. This implies that the  $X_0(\text{In})$  does not possess an intrinsic dipole moment, in contrast to IX, or that its dipole moment is induced by  $E_h$  due to a symmetric and nearly spherical distribution of charges in the absence of the electric field. This contrasting behavior between  $X_0(\text{In})$  and IX further supports the notion of IX being indeed an interlayer exciton emission from the interface between both compounds.

**Evidence for Energy Quantization.** Having provided enough experimental evidence to support the presence of a pronounced interlayer exciton emission IX in  $\gamma$ -InSe/ $\epsilon$ -GaSe heterostructures, we proceed to discuss its structure which, as shown below and in sharp contrast to the emissions discussed in Figure S7, is composed of several superimposed emissions which are nearly equally spaced in energy, as if quantized. Energy quantization would result from excitons localized at the moiré potential minima of twisted bilayers.<sup>19,22,52</sup> Nevertheless, despite the number of reports claiming to observe so-called moiré excitons, the community is not yet in position to discard other possible interpretations, such as phonon-mediated states, defect-bound states, or spin triplet states.<sup>37–40,56</sup> Unambiguous evidence for moiré trapped excitons would require the ability to image the optical response of individual mini moiré Brillouin zones, and confirm its reproducibility throughout the entire interfacial area of the heterostructure. Ours, as well as the experimental set-ups used by other groups, focus the impinging light excitation into spots having a typical diameter of  $\sim 1$   $\mu\text{m}$ . This spot area is considerably larger than the typical moiré periodicity  $\lambda$ , which ranges between one and tens of nanometers, implying that the incoming light excites thousands of moiré unit cells. Nevertheless, we show below that the structure of IX, collected from different points at the interface, is quite reproducible

A sketch of a 1L- $\gamma$ -InSe stacked onto 1L- $\epsilon$ -GaSe forming a small  $\phi$  between their main crystallographic axes (Figure 4a) illustrates the moiré periodicity  $\lambda$  resulting from modulations in the local stacking. According to ref 44, for our heterostructures  $\lambda$  would range from  $\sim 46$  Å (for  $\phi = 0^\circ$ ) to  $\sim 7$  Å (for  $\phi = 30^\circ$ ) (Figure 4b). To support our claim about the interlayer nature of the IX exciton emission centered at  $\sim 1.5$  eV for a 5L- $\epsilon$ -GaSe/4L- $\gamma$ -InSe heterostructure, we also measured its amplitude as a function of the laser excitation energy (i.e., from  $\sim 1.6$  to  $2.6$  eV, Figure 4c). The amplitude of the IX emission increases as the excitation energy surpasses  $1.7$  eV (corresponding to the  $X_0(\text{In})$  for 4L- $\gamma$ -InSe) reaching a plateau beyond  $\sim 2.1$  eV (the  $X_0(\text{Ga})$  emission for 5L- $\epsilon$ -GaSe). This implies that intralayer excitons from both layers contribute to IX as they decay. However, we did not observe

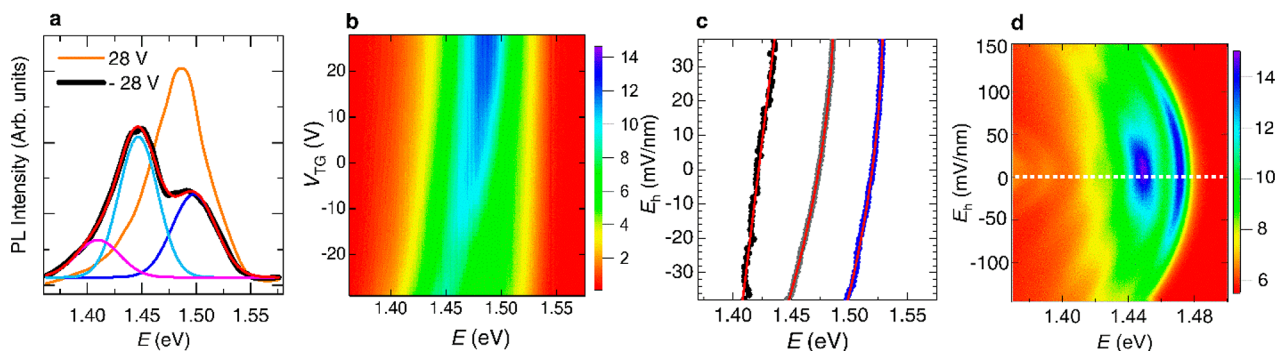


**Figure 3.** Role of electric field on both the interlayer and intralayer  $X_0(\text{In})$  exciton emissions. (a) Interlayer exciton emission from the 5L- $\epsilon$ -GaSe on 4L- $\gamma$ -InSe heterostructure ( $\phi \cong 23.4^\circ$ , see Figure S11) for three values of the top-gate voltage,  $V_{\text{TG}} = +28$  V (orange trace), and  $-28$  V (black markers). Magenta, light blue, and blue lines are Gaussian fits to the interlayer exciton emission under  $V_{\text{TG}} = -28$  V. Red line is their superposition. (b) Contour plot depicting the intensity of the interlayer exciton emissions IX illustrating their mild nonlinear response (blue shift) as  $V_{\text{TG}}$  (or electric field) is varied. (c) Center of the fitted Gaussians (in eV) as  $V_{\text{TG}}$  is tuned. The emission at the lowest energy (black markers) can be well-described by a linear fit (red line), while those at higher energies (gray and blue markers) are described by a linear plus a negative quadratic term corresponding to the second-order Stark shift correction (dark magenta line). Here, the electric field  $E_h$  is given by  $E_h = V_{\text{TG}}/t \times \epsilon(h\text{-BN})/\epsilon(\text{InSe-GaSe})$  where the dielectric constant  $\epsilon(h\text{-BN}) \approx \epsilon(\text{SiO}_2) \approx 3.7$  and  $\epsilon(\text{InSe-GaSe})$  is the average value between  $\epsilon(\text{InSe}) = 7.6$  and  $\epsilon(\text{GaSe}) = 6.1$  or 6.85. From the linear fit we calculate the electric dipolar moment  $\mu_e = e \cdot d$ , yielding an electron–hole separation  $d = (3.6 \pm 0.1)$  Å, which is close to the calculated value of 3.4 Å for the interlayer Se separation at the interface. This value increases by  $\sim 35\%$  for the emission at the highest energy. (d) Intensity of the intralayer exciton emission of InSe,  $X_0(\text{InSe})$ , as a function of  $E_h$  for a 5L- $\gamma$ -InSe crystal encapsulated among  $h$ -BN layers in a double gated configuration. The intensity of  $X_0(\text{InSe})$  is symmetric with respect to positive and negative values of  $E_h$  displaying a quadratic dependence on  $E_h$ . Such dependence, which is consistent with the nonlinear Stark effect, is observed in nearly isotropic excitons whose dipole moment is induced by the external electric field. This contrasting behavior between IX and  $X_0(\text{In})$  confirms that the former emission cannot be attributed to the original  $X_0(\text{In})$  when subjected to the distinct dielectric environment of the heterostructure.

clear PL peaks at the absorption energies corresponding to each intralayer emission. The reason for this is not clear, although it points to very fast intralayer exciton decays via interlayer recombination processes.

As mentioned previously, the IX emission from twisted  $\gamma$ -InSe/ $\epsilon$ -GaSe heterostructures can be decomposed into several peaks. This implies the superposition of multiple emissions as claimed for excitons trapped by the moiré potential in twisted TMDs.<sup>19,21–25,16</sup> To illustrate this point, we fit the IX emissions (Figure 4d–f), from three distinct heterostructures characterized by different constituent layer thicknesses and twist angles (i.e.,  $\phi = 0.3, 23.4,$  and  $47.9^\circ$ ) as determined through second harmonic generation measurements (Figure S9–S14), to a minimum set of three Gaussians that satisfactorily describe these IX emissions. The reason for choosing three Gaussian functions is illustrated by the fits in Figure S7: Three Gaussians are needed for a proper fit of the IX emissions while also capturing in certain heterostructures the very weak  $X_0(\text{In})$  emission in the vicinity of IX. In contrast to the PL spectra shown in Figure S7d,e whose  $X_0(\text{In})$  emissions are not only weak but also well-separated from IX, for the three heterostructures whose deconvoluted IX emissions are shown in Figure 4d–f,  $\Delta E$  remains nearly constant as if resulting from energy quantization.  $\Delta E$  increases from an average value of  $\sim 15$  to  $\sim 52$  meV as  $\phi$  increases from 0.3 to  $47.9^\circ$  indicating that their envelopes broaden considerably upon increasing  $\phi$ , implying that they are particularly sensitive with respect to the twist angle. These observations would be compatible with energy quantization due to exciton localization induced by a moiré potential whose periodicity  $\lambda$  is defined  $\phi$ . Notice that the values of  $\Delta E$  extracted here are comparable to  $\Delta E \sim 20$  meV typical for the IX emissions from TMD hetero-bilayers that are indeed characterized by a moiré periodicity.<sup>22</sup> In Figure 4, the reason for including results from heterostructures assembled from

layers having quite disparate thicknesses (e.g., Figure 4e,f) is to clearly illustrate two points: (i) that the position in energy of the IX emission is clearly layer-thickness-dependent and (ii) that the overall width of the IX emission is clearly twist-angle-dependent.

Importantly, our PL measurements performed at different locations throughout the interface reveal that the envelope of the IX emission is position-dependent but always well described by the same set of Gaussians with nearly constant  $\Delta E$  (Figure 4f). In a moiré interlayer exciton scenario, position-dependent emission amplitudes would be compatible with mild local strain<sup>57–59</sup> or modulations in the interlayer coupling associated with lattice relaxation that modulates their coupling to the moiré potential. Disorder, adsorbates, and polymer residues would be expected to produce random, position-dependent emissions in contrast to what is exposed here and to what was claimed for moiré excitons in TMDs.<sup>23</sup> One must bear in mind that the displacement of IX to higher energies (Figure 1e) as the thicknesses of the constituent layers decrease, or as the  $\gamma$ -InSe and  $\epsilon$ -GaSe direct gaps increase,<sup>35</sup> can only be reconciled with the IX emissions being intrinsic to the heterostacks instead of (random) emissions from defects.

We also argue that these IX emissions cannot be associated with bulk emissions resulting from, for instance, phonon replicas or other bulk processes.<sup>60</sup> To support this argument, we evaluated the PL spectra from bulk  $\gamma$ -InSe at  $T = 300$  K as well as  $T = 5$  K (Figure S15), from encapsulated 5L- $\gamma$ -InSe (Figure S16), and bulk  $\epsilon$ -GaSe at  $T = 5$  K (Figure S17). In all cases, the amplitude of the individual intralayer emissions (fitted to Lorentzian functions) increase as the energy increases, in sharp contrast to what is seen in Figure 4d–f for IX. In addition, the emissions from  $\epsilon$ -GaSe are observed to be *not* equidistant in energy, as in the case for those from IX, being observed at much higher energies than the IX emissions. Furthermore, at  $T = 5$  K the emissions from  $\gamma$ -InSe become

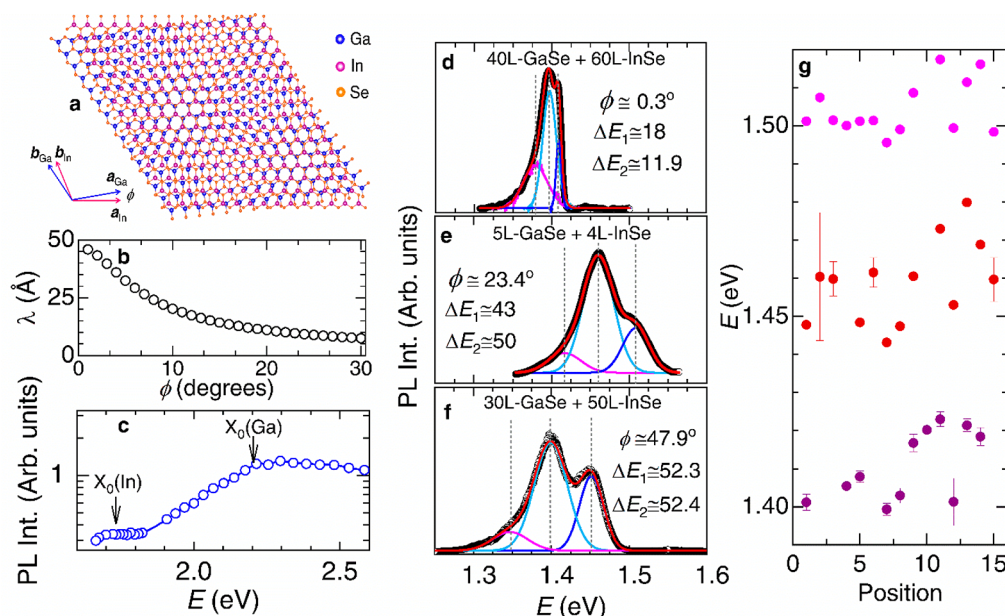


**Figure 4.** Twist-angle-dependent interlayer IX exciton emissions and evidence for energy quantization. (a) Depiction of 1L- $\gamma$ -InSe superimposed onto 1L- $\epsilon$ -GaSe forming a relative twist angle  $\phi$ . Here, blue, magenta, and orange spheres depict Ga, In, and Se atoms, respectively. The twist angle leads to a longer range periodicity that produces a moiré potential pinning excitons or photogenerated bound electron–hole pairs. (b) Moiré periodicity  $\lambda$  as a function of the twist angle  $\phi$  for 1L- $\epsilon$ -GaSe/1L- $\gamma$ -InSe heterostructures. (c) Intensity of the photoluminescent peak centered at  $\sim 1.5$  eV that is associated with the interlayer exciton IX emission of a 4L- $\gamma$ -InSe on 5L- $\epsilon$ -GaSe heterostructure as a function of the excitation energy  $E$ . Notice that the intensity of IX increases as the excitation energy surpasses 1.7 eV, the value corresponding to the intralayer exciton  $X_0$ (In) of 4L- $\gamma$ -InSe but plateaus beyond  $\sim 2.1$  eV, the energy required to excite the  $X_0$ (Ga) of 5L- $\epsilon$ -GaSe. This enhancement of IX upon excitation of all exciton states confirms its interlayer nature and indicates that all emissions are intrinsic to the strongly coupled InSe/GaSe heterostructure.<sup>21</sup> (d) to (f) Photoluminescent spectra from three  $n$ (Ga)L- $\epsilon$ -GaSe/ $n$ (In)L- $\gamma$ -InSe heterostructures having, according to second harmonic generation, twist angles  $\phi = (0.3 \pm 0.5)$ ,  $(23.4 \pm 1.7)$ , and  $(47.9 \pm 1.1)^\circ$  respectively (see Figures S8, S10, and S11 for the determination of  $\phi$ ). The spectra (black markers) can be fit to a minimal set of three Gaussians (magenta, light blue, and blue lines) describing emissions at distinct energies. Red line corresponds to their superposition. Notice how their separation in energy  $\Delta E$ , given in meV and indicated by vertical dotted gray lines, increases with  $\phi$ . As illustrated by the sample in panel (f), regardless of the precise laser spot coordinates, every emission can be characterized by a minimum set of three energy levels, as illustrated by our fits to three Gaussians. (g) Center of the Gaussians for the 5L- $\epsilon$ -GaSe on 4L- $\gamma$ -InSe heterostructure ( $\phi \cong 23.4^\circ$ ) as a function of the position, indicating that they are separated by about  $\sim 50$  meV regardless of laser spot position. The scattering in energy among these points would suggest an inhomogeneous moiré lattice.

considerably narrower than those from IX as seen in Figure 4d–f. In addition, and as seen in Figure S16, the individual emissions from bulk and thin exfoliated  $\gamma$ -InSe are considerably sharper (i.e.,  $\sim 14$  meV at fwhm for the bulk and  $\sim 5$  meV at fwhm for the exfoliated crystal) with respect to those of IX shown in Figure 4, which range from 20 and 50 meV at fwhm. All these observations, indicate that the splitting of the IX emissions have a distinct origin with respect to the emissions observed in the original compounds.

Notice that by moving the laser spot to the edge of the 5L- $\gamma$ -InSe encapsulated crystal we observe fairly narrow random emissions (whose full width at half-maximum is  $< 1$  meV) that are akin to those seen in ref 23 which, in contrast, we associate to edge defects or broken bonds resulting from the exfoliation process. Nevertheless, these IX emissions emerge only below  $T < 80$  K (Figure S18) confirming that they are not intrinsic to the original bulk compounds. However, IX blue-shifts and saturates as the illumination power increases (Figure S19), and this is precisely what is expected for interlayer excitons dominated by Coulomb like dipole–dipole interactions.<sup>49</sup>

To first approximation, the energy quantization of the IX emissions can be understood in terms of excitons trapped by a parabolic potential (e.g., describing the confinement within a moiré potential minima). Excitons can be treated as wave-

packets that move through a “pinning” potential with the motion of their center of mass described by<sup>22</sup>

$$V = V_0 + \hbar^2 k^2 / 2M + V_m(x, y) \quad (1)$$

Here,  $V_0$  is a constant given by the energy gap associated with the type-II band alignment,  $\hbar^2 k^2 / 2M$  is the kinetic energy of the exciton center of mass, and  $V_m(x, y)$  describes the potential minima (e.g., produced by the moiré periodicity). In the strong coupling regime,  $V_m(x, y) = m\omega_0^2(x^2 + y^2)/2$ , where  $\omega_0$  is the eigenfrequency within the harmonic trap and  $m$  is the exciton effective mass. Such potential would lead to twist-angle-dependent eigenenergies that would indeed be quantized, as seen experimentally:<sup>22</sup>

$$E_{n_x, n_y}(\phi) = E_0 + \hbar\omega_0(\phi)[n_x + n_y] \quad (2)$$

Although the evidence provided here is consistent with localized excitons displaying quantized energy levels, we are not yet in position to solidly claim that this arises from the moiré periodicity. This would require a precise determination of the IX planar radius via, for example, measurements of the diamagnetic shift under very high magnetic fields,<sup>61</sup> to compare it with the moiré periodicity  $\lambda(\phi)$  (Figure 4b).

Notice that a measured dipole separation of  $d \cong 0.36$  nm is considerably smaller (by nearly 1 order of magnitude) than the

typical IX radii ( $\sim 1.6$  nm) extracted from TMDs encapsulated among *h*-BN layers.<sup>42</sup> This dimension is also smaller than the calculated moiré periodicity as a function of  $\phi$  (Figure 4b), indicating that a nearly isotropic *s*-wave exciton could become pinned by the potential minima associated with the rather small moiré periodicities intrinsic to the  $\gamma$ -InSe/ $\epsilon$ -GaSe heterostructures. Nevertheless, more work is needed to verify this tantalizing possibility by focusing on a comparison between the planar dimensions of IX relative to the moiré periodicity  $\lambda$  of a given heterostructure. We finalize by mentioning that the intralayer excitons have also been reported to be particularly susceptible to the moiré potential.<sup>21</sup> In fact, there are multiple superimposed emissions also for  $X_0$ (Ga) that are fairly reproducible throughout the interface between both compounds (Figures S19 and S20).

## CONCLUSIONS

In summary, we report a pronounced interlayer exciton emission in metal monochalcogenide heterostructures at low temperatures, whose energy is layer-thickness-dependent and whose width (in energy) is twist-angle-dependent. The overall phenomenology unveiled here is similar to previous reports on excitons subjected to the moiré potential intrinsic to twisted bilayers of transition metal dichalcogenides. However, and in contrast to TMDs, this very pronounced interlayer emission occurs over the entire range of twist angles and a broad variation in layer thicknesses. We argue that its existence is attributable to the direct band gap at Brillouin zone center that is intrinsic to multilayered metal monochalcogenides.

At this point, it is quite important to clarify the origin of its quite reproducible multicomponent emissions. These cannot be attributed to phonon replicas given that replicas would not lead to nearly equidistant (in energy) emissions, or defects and adsorbates at the interface that would lead to random emissions as a function of interfacial spatial coordinates, in clear contrast to our observations. Should these emissions result from exciton localization due to the underlying moiré potential it would imply the existence of interlayer excitons with small radii in metal monochalcogenide heterostructures.

In effect, as discussed in ref 18, an uniform and ordered array of nanodots (e.g., excitons trapped by a moiré potential) could be utilized for semiconductor lasers or as single-photon emitters. Artificial lattices of interacting quasiparticles also offer a potential for applications in quantum information processing, through the creation of coherent exciton condensates, with  $\gamma$ -InSe/ $\epsilon$ -GaSe heterostructures offering a high level of tunability of their optical response with an intrinsic electric field at their interface that would find natural applications in, for instance, photovoltaics. Upon charge carrier doping, it might be possible to induce a complex, twist-angle-dependent phase-diagram containing correlated electronic phases.<sup>62</sup> Furthermore, the optical tunability intrinsic to metal monochalcogenides can be further enhanced by creating stacks with their S or Te analogs, or even transition metal dichalcogenides.<sup>63</sup>

## METHODS

**Single-Crystal Synthesis.** InSe single crystals were grown through the Bridgman method: The 6N-pure indium and 5N-pure selenium pellets in an atomic ratio of 52:48 were sealed in an evacuated quartz ampule and subsequently placed into a radio frequency (RF) furnace where the RF power was gradually increased to raise the temperature up to 800 °C. The ampule was then pulled through the hottest zone at a rate of 2 mm/hour. Single crystals were

characterized via electron-dispersive spectroscopy and aberration corrected transmission electron microscopy. Single crystals of GaSe were grown via a Ga flux method: Ga (6N) and Se (5N) in a ratio of 10:1 were sealed in a quartz ampule and heated up to 1000 °C, subsequently slowly cooled down to 400 °C, and then centrifuged. The *h*-BN crystals were produced by precipitation from molten metal solutions at atmospheric pressure.<sup>64</sup>

**X-ray Diffraction.** Single crystals of GaSe were cut to appropriate sizes and mounted on glass fibers with two-part epoxy. Data were collected with a Bruker D8 Quest Kappa single-crystal X-ray diffractometer with a Mo  $K\alpha$   $1\mu$ S microfocus source, a HELIOS optics monochromator, and Photon 100 CMOS detector. Absorption corrections were performed using the Bruker SADABS program (multiscan method).<sup>65</sup> Starting crystallographic models were obtained using the intrinsic phasing method in SHELXT<sup>66</sup> and atomic sites were refined anisotropically using SHELXL2014.<sup>67</sup> X-ray diffraction confirmed that the GaSe adopts the space group 187 ( $P6m2$ ) with lattice parameters  $a = 3.7557(3)$  Å and  $c = 15.9502(12)$  Å.  $\gamma$ -InSe adopts the  $R3m$  space group (160) with cell dimensions  $a = 4.08(2)$  Å and  $c = 24.938(24)$  Å.

**Heterostructure Fabrication.** Each constituent thin layer in the heterostructure, as well as the electrical gates, were exfoliated from bulk single-crystals onto polydimethylsiloxane (PDMS). A dry-transfer method within an Ar-filled glovebox was used to assemble stacks composed of few-layer graphene/*h*-BN/GaSe/InSe/*h*-BN. The PDMS stamp containing the above heterostructure was then stamped onto a 285 nm thick SiO<sub>2</sub> layer on a p-doped silicon substrate. A top graphene gate was electrically contacted through Cr/Au electrodes using electron-beam lithography and electron-beam evaporation techniques.

### Photoluminescence Measurements at Low Temperatures.

The photoluminescence measurements were performed in a Quantum Design Physical Properties Measurement System having a magnet that provides a maximum field  $\mu_0 H = 14$  T coupled to a custom probe containing a piezo stack that translates the sample under the objective of the microscope. The excitation provided by a continuous-wave laser excitation with a photon energy of 2.41 eV (514 nm wavelength) was used. The excitation light was focused through an objective (NA = 0.65) to a spot size of  $\sim 2$   $\mu$ m. The PL emission light was collected by the same objective and detected by a spectrometer equipped with a thermoelectrically cooled charge-coupled device (CCD) camera. The spectra presented throughout this manuscript were collected at several temperatures and recorded with a spectral resolution of 0.11 meV.

**Time-Resolved Photoluminescence.** Time-resolved PL measurements were performed at  $T = 5$  K using laser wavelength  $\lambda = 515$  nm with a power of 500  $\mu$ W. We checked that lower and higher illumination powers yielded similar lifetimes. For interlayer lifetime measurements, we excite the sample with a  $\tau < 200$  fs pulsed laser (Light Conversion PHAROS). Interlayer PL is spectrally filtered through a 0.5 m monochromator (Teledyne Princeton Instruments SpectraPro HRS-500) and detected with a fast time-correlated single-photon counting system composed of a fast (<30 ps full width at half-maximum) single-photon avalanche detector (Micro Photon Device PDM Series) and a picosecond event timer (PicoHarp 300).

**Second-Harmonic Generation (SHG) Measurements.** Linearly polarized, optical pulses with a central wavelength of 800 nm and average pulse duration of  $\sim 60$  fs were generated with a Ti:sapphire laser operating at a repetition rate of 5.1 MHz. Pulses were guided through a motorized half-wave-plate and focused at normal incidence through an objective lens (20 $\times$ , NA = 0.45) down to a  $1/e^2$  spot size of  $\sim 6$   $\mu$ m. The incident power at the sample was measured to be  $\sim 1$  mW. The sample-generated SHG light at 400 nm was collected by the same objective lens, passed through an analyzer (to select p or s output polarizations), and digitized into TTL pulses using a photomultiplier tube (Hamatsu H7360 series). Any undesired 800 nm light reflected back from the sample was removed prior to SHG detection via narrow-edge 400 nm bandpass filters. TTL counts were recorded as a function of half-wave-plate angular position, using a gated photon counter (Stanford Research Systems, SR400). All measurements were performed at room temperature and the second-

quadratic nature of the detected signal was verified through the quadratic dependence of SHG intensity on the incident power.

**Twist Angle Determination from SHG Measurements.** Twist angle values were determined from measured SHG patterns by deriving an optical response model for each material layer and fitting the resulting equations to the experimental data. More specifically, the polarization of a material layer  $P_M^{(2)}$  was first related to the electric field of the incident laser  $E_L$ , via

$$P_M^{(2)} = 2\epsilon_0 d_{i,l} \cdot E_L \cdot E_L$$

where  $\epsilon_0$  is the permittivity of free space and  $d_{i,l}$  represents the second-order, nonlinear optical susceptibility of the material, written in contracted notation. The electric field vector of the laser  $E_L$  was further decomposed into the analyzer's basis:

$$E_L = \begin{pmatrix} E_{L,0} \cos(\theta) \\ E_{L,0} \sin(\theta) \\ 0 \end{pmatrix}$$

Here,  $E_{L,0}$  denotes the electric field strength of the laser and  $\theta$  is the angle formed between horizontal axis of the analyzer's frame of reference (i.e., p-polarized direction) and the orientation of the electric field vector. Under this assumption, the calculated SHG polar patterns exhibit four lobes, similar to the recorded signals.

In order to also account for the optical response of a second, rotated material layer, a second basis was added to the model and rotated by a twist angle  $\alpha$  away from the analyzer's horizontal axis. Using the appropriate form of the  $d_{i,l}$  tensors associated with the crystallographic point groups of  $\gamma$ -InSe (i.e., trigonal  $3m$ ) and  $\epsilon$ -GaSe (i.e., hexagonal  $P6m2$ ), the polarization-dependent SHG intensities were found to be proportional to

$$I_{\text{InSe}}^p \propto (d_{\text{InSe}} \cos(2\theta + \delta))^2$$

$$I_{\text{InSe}}^s \propto (d_{\text{InSe}} \sin(2\theta + \delta))^2$$

$$I_{\text{GaSe}}^p \propto (d_{\text{GaSe}} \cos(2\theta + \delta - 3\alpha))^2$$

$$I_{\text{GaSe}}^s \propto (d_{\text{GaSe}} \sin(2\theta + \delta - 3\alpha))^2$$

where  $\delta$  was included as an additional fitting parameter to account for arbitrary crystallite orientations with respect to the laser's polarization direction.

For each sample,  $\delta$  was found by moving the laser spot above a heterostructure-free region of  $\gamma$ -InSe, capturing a SHG polar pattern while keeping the analyzer's position fixed and fitting the appropriate equation from our optical response model to the measured data. A similar procedure was repeated on a heterostructure-free region of  $\epsilon$ -GaSe, in order to determine twist angles, up to modulo  $60^\circ$ . The error incurred during the fitting procedure was estimated with a twist-angle-dependent, root-mean-square-error (RMSE) analysis of the form:

$$\text{RMSE} = \sqrt{\frac{\sum_{i=1}^n (y'_i - y_i)^2}{n}}$$

where  $n$  represents the total number of data points,  $y'_i$  are experimentally measured SHG intensities and  $y_i$  are the corresponding SHG intensity predictions given by the previous model. Each of the RMSE curves plotted against twist angles in the domain  $0^\circ$  to  $60^\circ$  exhibits a single, sharp minimum at the respective best fits for  $\alpha$ . The interval formed by the two twist angle values at twice the  $y$ -value of the best fit for  $\alpha$  correspond to a 95% confidence interval (i.e.,  $2\sigma$ ).

Twist angles close to  $0^\circ$  were further differentiated from those closer to  $60^\circ$  by moving the laser spot to location above the heterostructure region, and scanning the SHG polar pattern for the maximum SHG response: Heterostructures with twist angles closer to  $0^\circ$  show an enhanced SHG response due to constructive interference, whereas those with twist angles closer to  $60^\circ$  destructively interfere and do not exhibit any measurable SHG signal.<sup>68</sup> Our measurements still exhibit an uncertainty of  $2\sigma$  for twist angles close to  $30^\circ$ , where

heterostructures display maximal SHG responses that are similar in magnitude.<sup>68</sup>

**Theoretical Band Structure Calculations.** Calculations were performed using the VASP code<sup>69</sup> using a  $11 \times 11 \times 1$   $k$ -sampling grid. The energy cutoff is set to 500 eV, with a convergence criteria of  $10^{-8}$  eV and for the forces to 0.01 eV/Å. In order to avoid interactions between the layers, we applied periodic boundary conditions with a vacuum space of 25 Å. We used the projector augmented wave (PAW)<sup>70</sup> methods with a plane wave basis. We also took into account a fractional component of the exact exchange from the Hartree–Fock (HF) theory hybridized with the density functional theory (DFT) exchange–correlation functional at the level of the range-separated HSE06 hybrid functional<sup>71</sup> to extract the band structures included in the manuscript.

## ASSOCIATED CONTENT

### Supporting Information

The Supporting Information is available free of charge at <https://pubs.acs.org/doi/10.1021/acsnano.2c07394>.

Single-crystal X-ray diffraction pattern along the (00l) direction for a GaSe single crystal grown through a Ga flux method, relative band alignments between 3L- $\epsilon$ -GaSe and 3L- $\gamma$ -InSe, electronic charge density across the  $\gamma$ -InSe/ $\epsilon$ -GaSe interface, electronic potential across the  $\gamma$ -InSe/ $\epsilon$ -GaSe interface, electric field across the  $\gamma$ -InSe/ $\epsilon$ -GaSe interface, comparison between interlayer and intralayer exciton emissions in thick  $\gamma$ -InSe/ $\epsilon$ -GaSe heterostructures, deconvolution of the interlayer exciton emission for the multiple heterostructures shown in Figure 1, photoluminescence spectra from a non-annealed 4- $\gamma$ -InSe/4L- $\epsilon$ -GaSe heterostructure, determination of the twist angle for several heterostructures through second harmonic generation, photoluminescent emission from bulk  $\gamma$ -InSe, photoluminescence spectrum from few 5L- $\gamma$ -InSe at  $T = 5$ , photoluminescence spectrum at  $T = 5$  K for bulk  $\epsilon$ -GaSe grown via Ga flux, spectra of interlayer moiré emissions for several temperatures, intensity and position in energy of the interlayer moiré excitons as a function of the laser illumination power, observation of multiple emissions from the intralayer emission of GaSe at the interface, possible role for the moiré potential on the intralayer exciton emission of the  $\epsilon$ -GaSe layer, reproducibility of the intralayer exciton  $X_0(\text{Ga})$  emissions from  $\epsilon$ -GaSe (PDF)

## AUTHOR INFORMATION

### Corresponding Author

Luis Balicas – National High Magnetic Field Laboratory, Tallahassee, Florida 32310, United States; Department of Physics, Florida State University, Tallahassee, Florida 32306, United States; [orcid.org/0000-0002-5209-0293](https://orcid.org/0000-0002-5209-0293); Email: [balicas@magnet.fsu.edu](mailto:balicas@magnet.fsu.edu)

### Authors

Wenkai Zheng – National High Magnetic Field Laboratory, Tallahassee, Florida 32310, United States; Department of Physics, Florida State University, Tallahassee, Florida 32306, United States

Li Xiang – National High Magnetic Field Laboratory, Tallahassee, Florida 32310, United States; Department of Physics, Florida State University, Tallahassee, Florida 32306, United States

**Felipe A. de Quesada** – *Stanford Institute for Materials and Energy Sciences, SLAC National Accelerator Laboratory, Menlo Park, California 94025, United States; Department of Materials Science and Engineering, Stanford University, Stanford, California 94305, United States; [orcid.org/0000-0002-2039-9915](https://orcid.org/0000-0002-2039-9915)*

**Mathias Augustin** – *Institute for Condensed Matter Physics and Complex Systems, School of Physics and Astronomy and Higgs Centre for Theoretical Physics, The University of Edinburgh, Edinburgh EH9 3FD, United Kingdom*

**Zhengguang Lu** – *National High Magnetic Field Laboratory, Tallahassee, Florida 32310, United States; Department of Physics, Florida State University, Tallahassee, Florida 32306, United States; Present Address: Department of Physics, Massachusetts Institute of Technology, Cambridge, MA 02139, USA*

**Matthew Wilson** – *Department of Physics and Astronomy, University of California, Riverside, California 92521, United States*

**Aditya Sood** – *Stanford Institute for Materials and Energy Sciences, SLAC National Accelerator Laboratory, Menlo Park, California 94025, United States; Department of Materials Science and Engineering, Stanford University, Stanford, California 94305, United States; [orcid.org/0000-0002-4319-666X](https://orcid.org/0000-0002-4319-666X)*

**Fengcheng Wu** – *School of Physics and Technology, Wuhan University, Wuhan 430072, China*

**Dmitry Shcherbakov** – *Department of Physics, The Ohio State University, Columbus, Ohio 43210, United States*

**Shahriar Memaran** – *National High Magnetic Field Laboratory, Tallahassee, Florida 32310, United States; Department of Physics, Florida State University, Tallahassee, Florida 32306, United States*

**Ryan E. Baumbach** – *National High Magnetic Field Laboratory, Tallahassee, Florida 32310, United States; Department of Physics, Florida State University, Tallahassee, Florida 32306, United States*

**Gregory T. McCandless** – *Department of Chemistry and Biochemistry, Baylor University, Waco, Texas 76798, United States*

**Julia Y. Chan** – *Department of Chemistry and Biochemistry, Baylor University, Waco, Texas 76798, United States; [orcid.org/0000-0003-4434-2160](https://orcid.org/0000-0003-4434-2160)*

**Song Liu** – *Tim Taylor Department of Chemical Engineering, Kansas State University, Manhattan, Kansas 66506, United States*

**James H. Edgar** – *Tim Taylor Department of Chemical Engineering, Kansas State University, Manhattan, Kansas 66506, United States*

**Chun Ning Lau** – *Department of Physics, The Ohio State University, Columbus, Ohio 43210, United States; [orcid.org/0000-0003-2159-6723](https://orcid.org/0000-0003-2159-6723)*

**Chun Hung Lui** – *Department of Physics and Astronomy, University of California, Riverside, California 92521, United States*

**Elton J. G. Santos** – *Institute for Condensed Matter Physics and Complex Systems, School of Physics and Astronomy and Higgs Centre for Theoretical Physics, The University of Edinburgh, Edinburgh EH9 3FD, United Kingdom; Donostia International Physics Centre, 20018 Donostia-San Sebastian, Spain*

**Aaron Lindenberg** – *Stanford Institute for Materials and Energy Sciences, SLAC National Accelerator Laboratory,*

*Menlo Park, California 94025, United States; Department of Materials Science and Engineering, Stanford University, Stanford, California 94305, United States; [orcid.org/0000-0003-3233-7161](https://orcid.org/0000-0003-3233-7161)*

**Dmitry Smirnov** – *National High Magnetic Field Laboratory, Tallahassee, Florida 32310, United States; [orcid.org/0000-0001-6358-3221](https://orcid.org/0000-0001-6358-3221)*

Complete contact information is available at:  
<https://pubs.acs.org/10.1021/acsnano.2c07394>

### Author Contributions

W.Z. and L.B. conceived the project. W.Z. fabricated the heterostructures. W.Z., L.X., Z.L., D.S., and M.W. performed photoluminescence measurements. W.Z., F.W., and L.B. analyzed and interpreted the data. W.Z., S.M., and L.B. synthesized the  $\gamma$ -InSe and  $\epsilon$ -GaSe single-crystals. S.L. and J.E. provided the h-BN crystals. G.T.M. and J.Y.C. performed the structural studies. E.S. and M.A. provided the theoretical calculations. F.d.Q., A.S., and A.L. performed the second harmonic generation measurements and analysis to extract the twist angle. M.W. performed time-dependent photoluminescence measurements. W.Z. and L.B. wrote the manuscript with the input of all coauthors. All authors discussed and commented on the manuscript.

### Notes

The authors declare no competing financial interest.

### ACKNOWLEDGMENTS

We acknowledge Justin B. Felder for assistance in collecting single crystalline X-ray data and Alex Moon for assistance in heterostructure fabrication. L.B. acknowledges support from US NSF-DMR 2219003 (synthesis, physical characterization, and heterostructure fabrication) and the Office Naval Research DURIP Grant 11997003 (stacking under inert conditions). L.B. also acknowledges the hospitality of the Aspen Center for Physics, which is supported by US NSF grant PHY-1607611. C.N.L. acknowledges US NSF-DMR 2219048. J.Y.C. acknowledges support from NSF DMR 2209804 and Welch Foundation AT-2056-20210327. R.E.B. acknowledges support from the National Science Foundation through NSF-DMR1904361. The crystal growth (S.L. and J.E.) in this study was supported by the Materials Engineering and Processing program of the National Science Foundation, Award No. CMMI 1538127. F.Q., A.S., and A.L. acknowledge support from the US Department of Energy (DOE), Office of Basic Energy Sciences, Division of Materials Sciences and Engineering, under contract no. DE-842 AC02-76SF00515. D.S. acknowledges support from the U.S. Department of Energy (DE-FG02-07ER46451) for photoluminescence measurements. C.H.L. acknowledges support from the National Science Foundation Division of Materials Research CAREER Award No. 1945660 and the American Chemical Society Petroleum Research Fund No. 61640-ND6. EJGS acknowledges computational resources through CIRRUS Tier-2 HPC Service (ec131 Cirrus Project) at EPCC (<http://www.cirrus.ac.uk>) funded by the University of Edinburgh and EPSRC (EP/P020267/1); ARCHER UK National Supercomputing Service (<http://www.archer.ac.uk>) via Project d429. E.S. acknowledges the Spanish Ministry of Science's grant program "Europa-Excelencia" under grant number EUR2020-112238, the EPSRC Early Career Fellowship (EP/T021578/1), and the University of Edinburgh for funding support. This work was supported by the US-NSF

(Platform for the Accelerated Realization, Analysis, and Discovery of Interface Materials (PARADIM)) under Cooperative Agreement No. DMR-2039380. The National High Magnetic Field Laboratory acknowledges support from the US-NSF Cooperative agreement Grant number DMR-1644779 and the state of Florida.

## REFERENCES

- (1) Butov, L. V.; Ivanov, A. L.; Imamoglu, A.; Littlewood, P. B.; Shashkin, A. A.; Dolgoplov, V. T.; Campman, K. L.; Gossard, A. C. Stimulated Scattering of Indirect Excitons in Coupled Quantum Wells: Signature of a Degenerate Bose-Gas of Excitons. *Phys. Rev. Lett.* **2001**, *86* (24), 5608–5611.
- (2) Fogler, M. M.; Butov, L. V.; Novoselov, K. S. High-temperature Superfluidity with Indirect Excitons in van der Waals Heterostructures. *Nat. Commun.* **2014**, *5* (1), 4555.
- (3) Combescot, M.; Combescot, R.; Dubin, F. Bose–Einstein Condensation and Indirect Excitons: a review. *Rep. Prog. Phys.* **2017**, *80* (6), 066501.
- (4) Schwartz, I.; Cogan, D.; Schmidgall, E. R.; Don, Y.; Gantz, L.; Kenneth, O.; Lindner, N. H.; Gershoni, D. Deterministic Generation of a Cluster State of Entangled Photons. *Science* **2016**, *354* (6311), 434–437.
- (5) Poem, E.; Kodriano, Y.; Tradonsky, C.; Lindner, N. H.; Gerardot, B. D.; Petroff, P. M.; Gershoni, D. Accessing the Dark Exciton with Light. *Nat. Phys.* **2010**, *6* (12), 993–997.
- (6) High, A. A.; Leonard, J. R.; Remeika, M.; Butov, L. V.; Hanson, M.; Gossard, A. C. Condensation of Excitons in a Trap. *Nano Lett.* **2012**, *12* (5), 2605–2609.
- (7) High, A. A.; Leonard, J. R.; Hammack, A. T.; Fogler, M. M.; Butov, L. V.; Kavokin, A. V.; Campman, K. L.; Gossard, A. C. Spontaneous Coherence in a Cold Exciton Gas. *Nature* **2012**, *483* (7391), 584–588.
- (8) High, A. A.; Thomas, A. K.; Grosso, G.; Remeika, M.; Hammack, A. T.; Meyertholen, A. D.; Fogler, M. M.; Butov, L. V.; Hanson, M.; Gossard, A. C. Trapping Indirect Excitons in a GaAs Quantum-Well Structure with a Diamond-Shaped Electrostatic Trap. *Phys. Rev. Lett.* **2009**, *103* (8), 087403.
- (9) High, A. A.; Hammack, A. T.; Butov, L. V.; Mouchliadis, L.; Ivanov, A. L.; Hanson, M.; Gossard, A. C. Indirect Excitons in Elevated Traps. *Nano Lett.* **2009**, *9* (5), 2094–2098.
- (10) Hammack, A. T.; Griswold, M.; Butov, L. V.; Smallwood, L. E.; Ivanov, A. L.; Gossard, A. C. Trapping of Cold Excitons in Quantum Well Structures with Laser Light. *Phys. Rev. Lett.* **2006**, *96* (22), 227402.
- (11) Butov, L. V.; Lai, C. W.; Ivanov, A. L.; Gossard, A. C.; Chemla, D. S. Towards Bose–Einstein Condensation of Excitons in Potential Traps. *Nature* **2002**, *417* (6884), 47–52.
- (12) Rapaport, R.; Chen, G.; Snoke, D.; Simon, S. H.; Pfeiffer, L.; West, K.; Liu, Y.; Denev, S. Charge Separation of Dense Two-Dimensional Electron-Hole Gases: Mechanism for Exciton Ring Pattern Formation. *Phys. Rev. Lett.* **2004**, *92* (11), 117405.
- (13) Hong, X.; Kim, J.; Shi, S.-F.; Zhang, Y.; Jin, C.; Sun, Y.; Tongay, S.; Wu, J.; Zhang, Y.; Wang, F. Ultrafast Charge Transfer in Atomically Thin MoS<sub>2</sub>/WS<sub>2</sub> Heterostructures. *Nat. Nanotechnol.* **2014**, *9* (9), 682–686.
- (14) Rivera, P.; Schaibley, J. R.; Jones, A. M.; Ross, J. S.; Wu, S.; Aivazian, G.; Klement, P.; Seyler, K.; Clark, G.; Ghimire, N. J.; Yan, J.; Mandrus, D. G.; Yao, W.; Xu, X. Observation of Long-Lived Interlayer Excitons in Monolayer MoSe<sub>2</sub>–WSe<sub>2</sub> Heterostructures. *Nat. Commun.* **2015**, *6* (1), 6242.
- (15) Unuchek, D.; Ciarrocchi, A.; Avsar, A.; Watanabe, K.; Taniguchi, T.; Kis, A. Room-Temperature Electrical Control of Exciton Flux in a van der Waals Heterostructure. *Nature* **2018**, *560* (7718), 340–344.
- (16) Golub, J. E.; Kash, K.; Harbison, J. P.; Florez, L. T. Long-lived Spatially Indirect Excitons in Coupled GaAs/Al<sub>x</sub>Ga<sub>1-x</sub>As Quantum Wells. *Phys. Rev. B* **1990**, *41* (12), 8564–8567.
- (17) Sun, Z.; Ciarrocchi, A.; Tagarelli, F.; Gonzalez Marin, J. F.; Watanabe, K.; Taniguchi, T.; Kis, A. Excitonic Transport Driven by Repulsive Dipolar Interaction in a van der Waals Heterostructure. *Nat. Photonics* **2022**, *16* (1), 79–85.
- (18) Brotons-Gisbert, M.; Baek, H.; Molina-Sánchez, A.; Campbell, A.; Scerri, E.; White, D.; Watanabe, K.; Taniguchi, T.; Bonato, C.; Gerardot, B. D. Spin–layer Locking of Interlayer Excitons Trapped in Moiré Potentials. *Nat. Mater.* **2020**, *19* (6), 630–636.
- (19) Yu, H.; Liu, G.-B.; Tang, J.; Xu, X.; Yao, W. Moiré Excitons: From Programmable Quantum Emitter Arrays to Spin-Orbit–Coupled Artificial Lattices. *Sci. Adv.* **2017**, *3* (11), e1701696.
- (20) Wu, F.; Lovorn, T.; MacDonald, A. H. Topological Exciton Bands in Moiré Heterojunctions. *Phys. Rev. Lett.* **2017**, *118* (14), 147401.
- (21) Jin, C.; Regan, E. C.; Yan, A.; Iqbal Bakti Utama, M.; Wang, D.; Zhao, S.; Qin, Y.; Yang, S.; Zheng, Z.; Shi, S.; Watanabe, K.; Taniguchi, T.; Tongay, S.; Zettl, A.; Wang, F. Observation of Moiré Excitons in WSe<sub>2</sub>/WS<sub>2</sub> Heterostructure Superlattices. *Nature* **2019**, *567* (7746), 76–80.
- (22) Tran, K.; Moody, G.; Wu, F.; Lu, X.; Choi, J.; Kim, K.; Rai, A.; Sanchez, D. A.; Quan, J.; Singh, A.; Embley, J.; Zepeda, A.; Campbell, M.; Autry, T.; Taniguchi, T.; Watanabe, K.; Lu, N.; Banerjee, S. K.; Silverman, K. L.; Kim, S.; Tutuc, E.; Yang, L.; MacDonald, A. H.; Li, X. Evidence for Moiré Excitons in van der Waals Heterostructures. *Nature* **2019**, *567* (7746), 71–75.
- (23) Seyler, K. L.; Rivera, P.; Yu, H.; Wilson, N. P.; Ray, E. L.; Mandrus, D. G.; Yan, J.; Yao, W.; Xu, X. Signatures of Moiré-Trapped Valley Excitons in MoSe<sub>2</sub>/WSe<sub>2</sub> Heterobilayers. *Nature* **2019**, *567* (7746), 66–70.
- (24) Alexeev, E. M.; Ruiz-Tijerina, D. A.; Danovich, M.; Hamer, M. J.; Terry, D. R.; Nayak, P. K.; Ahn, S.; Pak, S.; Lee, J.; Sohn, J. I.; Molas, M. R.; Koperski, M.; Watanabe, K.; Taniguchi, T.; Novoselov, K. S.; Gorbachev, R. V.; Shin, H. S.; Fal'ko, V. I.; Tartakovskii, A. I. Resonantly Hybridized Excitons in Moiré Superlattices in van der Waals Heterostructures. *Nature* **2019**, *567* (7746), 81–86.
- (25) Wang, L.; Shih, E. M.; Ghiotto, A.; Xian, L.; Rhodes, D. A.; Tan, C.; Claassen, M.; Kennes, D. M.; Bai, Y. S.; Kim, B.; Watanabe, K.; Taniguchi, T.; Zhu, X. Y.; Hone, J.; Rubio, A.; Pasupathy, A. N.; Dean, C. R. Correlated Electronic Phases in Twisted Bilayer Transition Metal Dichalcogenides. *Nat. Mater.* **2020**, *19* (8), 861–866.
- (26) Pan, Y.; Fölsch, S.; Nie, Y.; Waters, D.; Lin, Y.-C.; Jariwala, B.; Zhang, K.; Cho, K.; Robinson, J. A.; Feenstra, R. M. Quantum-Confined Electronic States Arising from the Moiré Pattern of MoS<sub>2</sub>–WSe<sub>2</sub> Heterobilayers. *Nano Lett.* **2018**, *18* (3), 1849–1855.
- (27) Zhang, C.; Chuu, C.-P.; Ren, X.; Li, M.-Y.; Li, L.-J.; Jin, C.; Chou, M.-Y.; Shih, C.-K. Interlayer Couplings, Moiré Patterns, and 2D Electronic Superlattices in MoS<sub>2</sub>/WSe<sub>2</sub> Hetero-bilayers. *Sci. Adv.* **2017**, *3* (1), e1601459.
- (28) Dean, C. R.; Wang, L.; Maher, P.; Forsythe, C.; Ghahari, F.; Gao, Y.; Katoch, J.; Ishigami, M.; Moon, P.; Koshino, M.; Taniguchi, T.; Watanabe, K.; Shepard, K. L.; Hone, J.; Kim, P. Hofstadter's Butterfly and the Fractal Quantum Hall Effect in Moiré Superlattices. *Nature* **2013**, *497* (7451), 598–602.
- (29) Cao, Y.; Fatemi, V.; Demir, A.; Fang, S.; Tomarken, S. L.; Luo, J. Y.; Sanchez-Yamagishi, J. D.; Watanabe, K.; Taniguchi, T.; Kaxiras, E.; Ashoori, R. C.; Jarillo-Herrero, P. Correlated Insulator Behaviour at Half-Filling in Magic-Angle Graphene Superlattices. *Nature* **2018**, *556* (7699), 80–84.
- (30) Cao, Y.; Fatemi, V.; Fang, S.; Watanabe, K.; Taniguchi, T.; Kaxiras, E.; Jarillo-Herrero, P. Unconventional Superconductivity in Magic-Angle Graphene Superlattices. *Nature* **2018**, *556* (7699), 43–50.
- (31) Sharpe, A. L.; Fox, E. J.; Barnard, A. W.; Finney, J.; Watanabe, K.; Taniguchi, T.; Kastner, M. A.; Goldhaber-Gordon, D. Emergent Ferromagnetism Near Three-Quarters Filling in Twisted Bilayer Graphene. *Science* **2019**, *365* (6453), 605–608.
- (32) Zheng, Z.; Ma, Q.; Bi, Z.; de la Barrera, S.; Liu, M.-H.; Mao, N.; Zhang, Y.; Kiper, N.; Watanabe, K.; Taniguchi, T.; Kong, J.; Tisdale, J.

- W. A.; Ashoori, R.; Gedik, N.; Fu, L.; Xu, S.-Y.; Jarillo-Herrero, P. Unconventional Ferroelectricity in Moiré Heterostructures. *Nature* **2020**, *588* (7836), 71–76.
- (33) Hejazi, K.; Luo, Z.-X.; Balents, L. Noncollinear Phases in Moiré Magnets. *Proc. Natl. Acad. Sci. U. S. A.* **2020**, *117* (20), 10721–10726.
- (34) Nayak, P. K.; Horbatenko, Y.; Ahn, S.; Kim, G.; Lee, J.-U.; Ma, K. Y.; Jang, A. R.; Lim, H.; Kim, D.; Ryu, S.; Cheong, H.; Park, N.; Shin, H. S. Probing Evolution of Twist-Angle-Dependent Interlayer Excitons in  $\text{MoSe}_2/\text{WSe}_2$  van der Waals Heterostructures. *ACS Nano* **2017**, *11* (4), 4041–4050.
- (35) Terry, D. J.; Zolyomi, V.; Hamer, M.; Tyurnina, A. V.; Hopkinson, D. G.; Rakowski, A. M.; Magorrian, S. J.; Clark, N.; Andreev, Y. M.; Kazakova, O.; Novoselov, K.; Haigh, S. J.; Fal'ko, V. I.; Gorbachev, R. Infrared-to-Violet Tunable Optical Activity in Atomic Films of GaSe, InSe, and their Heterostructures. *2D Mater.* **2018**, *5* (4), 041009.
- (36) Bandurin, D. A.; Tyurnina, A. V.; Yu, G. L.; Mishchenko, A.; Zolyomi, V.; Morozov, S. V.; Kumar, R. K.; Gorbachev, R. V.; Kudrynskiy, Z. R.; Pezzini, S.; Kovalyuk, Z. D.; Zeitler, U.; Novoselov, K. S.; Patane, A.; Eaves, L.; Grigorieva, I. V.; Fal'ko, V. I.; Geim, A. K.; Cao, Y. High Electron Mobility, Quantum Hall Effect and Anomalous Optical Response in Atomically Thin InSe. *Nat. Nanotechnol.* **2017**, *12* (3), 223–227.
- (37) Kumar, A. S.; Wang, M.; Li, Y.; Fujita, R.; Gao, X. P. A. Interfacial Charge Transfer and Gate-Induced Hysteresis in Monochalcogenide InSe/GaSe Heterostructures. *ACS Appl. Mater. Interfaces* **2020**, *12* (41), 46854–46861.
- (38) Mak, K. F.; Lee, C.; Hone, J.; Shan, J.; Heinz, T. F. Atomically Thin  $\text{MoS}_2$ : A New Direct-Gap Semiconductor. *Phys. Rev. Lett.* **2010**, *105* (13), 136805.
- (39) Casto, L. D.; Clune, A. J.; Yokosuk, M. O.; Musfeldt, J. L.; Williams, T. J.; Zhuang, H. L.; Lin, M. W.; Xiao, K.; Hennig, R. G.; Sales, B. C.; Yan, J. Q.; Mandrus, D. Strong Spin-Lattice Coupling in  $\text{CrSiTe}_3$ . *APL Mater.* **2015**, *3* (4), 041515.
- (40) Lu, Y.-Y.; Guo, C.-R.; Yeh, H.-L.; Chen, H.-W.; Kuo, C.-C.; Hsu, J.-H.; Jhou, J.; Huang, Y.-T.; Hsieh, S.-H.; Chen, C.-H.; Ho, C.-H.; Sankar, R.; Chou, F.-C. Multilayer GaSe/InSe Heterointerface-Based Devices for Charge Transport and Optoelectronics. *ACS Appl. Nano Mater.* **2020**, *3* (12), 11769–11776.
- (41) Yan, F.; Zhao, L.; Patanè, A.; Hu, P.; Wei, X.; Luo, W.; Zhang, D.; Lv, Q.; Feng, Q.; Shen, C.; Chang, K.; Eaves, L.; Wang, K. Fast, Multicolor Photodetection with Graphene-Contacted  $p$ -GaSe/ $n$ -InSe van der Waals Heterostructures. *Nanotechnology* **2017**, *28* (27), 27LT01.
- (42) Stier, A. V.; Wilson, N. P.; Clark, G.; Xu, X.; Crooker, S. A. Probing the Influence of Dielectric Environment on Excitons in Monolayer  $\text{WSe}_2$ : Insight from High Magnetic Fields. *Nano Lett.* **2016**, *16* (11), 7054–7060.
- (43) Shcherbakov, D.; Stepanov, P.; Memaran, S.; Wang, Y.; Xin, Y.; Yang, J.; Wei, K.; Baumbach, R.; Zheng, W.; Watanabe, K.; et al. Layer- and Gate-Tunable Spin-Orbit Coupling in a High-Mobility Few-Layer Semiconductor. *Sci. Adv.* **2021**, *7* (5), eabe2892.
- (44) Ribeiro-Palau, R.; Zhang, C.; Watanabe, K.; Taniguchi, T.; Hone, J.; Dean, C. R. Twistable Electronics with Dynamically Rotatable Heterostructures. *Science* **2018**, *361* (6403), 690–693.
- (45) Rivera, P.; Seyler, K. L.; Yu, H. Y.; Schaibley, J. R.; Yan, J. Q.; Mandrus, D. G.; Yao, W.; Xu, X. D. Valley-Polarized Exciton Dynamics in a 2D Semiconductor Heterostructure. *Science* **2016**, *351* (6274), 688–691.
- (46) Miller, B.; Steinhoff, A.; Pano, B.; Klein, J.; Jahnke, F.; Holleitner, A.; Wurstbauer, U. Long-Lived Direct and Indirect Interlayer Excitons in van der Waals Heterostructures. *Nano Lett.* **2017**, *17* (9), S229–S237.
- (47) Wang, J.; Ardelean, J.; Bai, Y. S.; Steinhoff, A.; Florian, M.; Jahnke, F.; Xu, X. D.; Kira, M.; Hone, J.; Zhu, X. Y. Optical Generation of High Carrier Densities in 2D Semiconductor Heterobilayers. *Sci. Adv.* **2019**, *5* (9), eaax0145.
- (48) Choi, J. H.; Hsu, W. T.; Lu, L. S.; Sun, L. Y.; Cheng, H. Y.; Lee, M. H.; Quan, J. M.; Tran, K.; Wang, C. Y.; Staab, M.; et al. Moiré Potential Impedes Interlayer Exciton Diffusion in van der Waals Heterostructures. *Sci. Adv.* **2020**, *6* (39), eaba8866.
- (49) Jauregui, L. A.; Joe, A. Y.; Pistunova, K.; Wild, D. S.; High, A. A.; Zhou, Y.; Scuri, G.; De Greve, K.; Sushko, A.; Yu, C.-H.; Taniguchi, T.; Watanabe, K.; Needleman, D. J.; Lukin, M. D.; Park, H.; Kim, P. Electrical Control of Interlayer Exciton Dynamics in Atomically Thin Heterostructures. *Science* **2019**, *366* (6467), 870–875.
- (50) Choi, J.; Florian, M.; Steinhoff, A.; Erben, D.; Tran, K.; Kim, D. S.; Sun, L.; Quan, J.; Claassen, R.; Majumder, S.; Hollingsworth, J. A.; Taniguchi, T.; Watanabe, K.; Ueno, K.; Singh, A.; Moody, G.; Jahnke, F.; Li, X. Twist Angle-Dependent Interlayer Exciton Lifetimes in van der Waals Heterostructures. *Phys. Rev. Lett.* **2021**, *126* (4), 047401.
- (51) Barre, E.; Karmi, O.; Liu, E.; O'Beirne, A. L.; Chen, X.; Ribeiro, H. B.; Yu, L.; Kim, B.; Watanabe, K.; Taniguchi, T.; et al. Optical Absorption of Interlayer Excitons in Transition-Metal Dichalcogenide Heterostructures. *Science* **2022**, *376* (6591), 406–410.
- (52) Huang, D.; Choi, J.; Shih, C. K.; Li, X. Q. Excitons in Semiconductor Moiré Superlattices. *Nat. Nanotechnol.* **2022**, *17* (3), 227–238.
- (53) Tang, Y.; Gu, J.; Liu, S.; Watanabe, K.; Taniguchi, T.; Hone, J.; Mak, K. F.; Shan, J. Tuning Layer-Hybridized Moiré Excitons by the Quantum-Confined Stark Effect. *Nat. Nanotechnol.* **2021**, *16* (1), S2–S7.
- (54) Leisgang, N.; Shree, S.; Paradisanos, I.; Sponfeldner, L.; Robert, C.; Lagarde, D.; Balocchi, A.; Watanabe, K.; Taniguchi, T.; Marie, X.; et al. Giant Stark Splitting of an Exciton in Bilayer  $\text{MoS}_2$ . *Nat. Nanotechnol.* **2020**, *15* (11), 901–907.
- (55) Hooker, A.; Greene, C. H.; Clark, W. Classical Examination of the Stark Effect in Hydrogen. *Phys. Rev. A* **1997**, *55* (6), 4609–4612.
- (56) Ciarrocchi, A.; Unuchek, D.; Avsar, A.; Watanabe, K.; Taniguchi, T.; Kis, A. Polarization Switching and Electrical Control of Interlayer Excitons in Two-Dimensional van der Waals Heterostructures. *Nat. Photonics* **2019**, *13* (2), 131–136.
- (57) Bai, Y.; Zhou, L.; Wang, J.; Wu, W.; McGilly, L. J.; Halbertal, D.; Lo, C. F. B.; Liu, F.; Ardelean, J.; Rivera, P.; Finney, N. R.; Yang, X.-C.; Basov, D. N.; Yao, W.; Xu, X.; Hone, J.; Pasupathy, A. N.; Zhu, X. Y. Excitons in Strain-Induced One-Dimensional Moiré Potentials at Transition Metal Dichalcogenide Heterojunctions. *Nat. Mater.* **2020**, *19* (10), 1068–1073.
- (58) Li, H.; Li, S.; Naik, M. H.; Xie, J.; Li, X.; Wang, J.; Regan, E.; Wang, D.; Zhao, W.; Zhao, S. Imaging Moiré Flat Bands in Three-Dimensional Reconstructed  $\text{WSe}_2/\text{WS}_2$  Superlattices. *Nat. Mater.* **2021**, *20*, 945–950.
- (59) Wei, T. R.; Jin, M.; Wang, Y. C.; Chen, H. Y.; Gao, Z. Q.; Zhao, K. P.; Qiu, P. F.; Shan, Z. W.; Jiang, J.; Li, R. B.; Chen, L. D.; He, J.; Shi, X. Exceptional Plasticity in the Bulk Single-Crystalline van der Waals Semiconductor InSe. *Science* **2020**, *369* (6503), 542–545.
- (60) Ferrer-Roca, C.; Segura, A.; Andres, M. V.; Pellicer, J.; Munoz, V. Investigation of Nitrogen-Related Acceptor Centers in Indium Selenide by Means of Photoluminescence: Determination of the Hole Effective Mass. *Phys. Rev. B* **1997**, *55* (11), 6981–6987.
- (61) Stier, A. V.; McCreary, K. M.; Jonker, B. T.; Kono, J.; Crooker, S. A. Exciton Diamagnetic Shifts and Valley Zeeman Effects in Monolayer  $\text{WS}_2$  and  $\text{MoS}_2$  to 65 T. *Nat. Commun.* **2016**, *7* (1), 10643.
- (62) Regan, E. C.; Wang, D.; Jin, C.; Bakti Utama, M. I.; Gao, B.; Wei, X.; Zhao, S.; Zhao, W.; Zhang, Z.; Yumigeta, K.; Blei, M.; Carlström, J. D.; Watanabe, K.; Taniguchi, T.; Tongay, S.; Crommie, M.; Zettl, A.; Wang, F. Mott and Generalized Wigner Crystal States in  $\text{WSe}_2/\text{WS}_2$  Moiré Superlattices. *Nature* **2020**, *579* (7799), 359–363.
- (63) Ubrig, N.; Ponomarev, E.; Zultak, J.; Domaretskiy, D.; Zolyomi, V.; Terry, D.; Howarth, J.; Gutierrez-Lezama, I.; Zhukov, A.; Kudrynskiy, Z. R.; Kovalyuk, Z. D.; Patane, A.; Taniguchi, T.; Watanabe, K.; Gorbachev, R. V.; Fal'ko, V. I.; Morpurgo, A. F. Design of van der Waals Interfaces for Broad-Spectrum Optoelectronics. *Nat. Mater.* **2020**, *19* (3), 299–304.
- (64) Liu, S.; He, R.; Ye, Z.; Du, X.; Lin, J.; Jiang, H.; Liu, B.; Edgar, J. H. Large-Scale Growth of High-Quality Hexagonal Boron Nitride

Crystals at Atmospheric Pressure from an Fe–Cr Flux. *Cryst. Growth Des.* **2017**, *17*, 4932–4935.

(65) Krause, L.; Herbst-Irmer, R.; Sheldrick, G. M.; Stalke, D. Comparison of Silver and Molybdenum Microfocus X-ray Sources for Single-Crystal Structure Determination. *J. Appl. Crystallogr.* **2015**, *48*, 3–10.

(66) Sheldrick, G. SHELXT - Integrated Space-Group and Crystal-Structure Determination. *Acta Crystallogr. A* **2015**, *71*, 3–8.

(67) Sheldrick, G. Crystal Structure Refinement with SHELXL. *Acta Crystallogr. C* **2015**, *71*, 3–8.

(68) Hsu, W.-T.; Zhao, Z.-A.; Li, L.-J.; Chen, C.-H.; Chiu, M.-H.; Chang, P.-S.; Chou, Y.-C.; Chang, W.-H. Second Harmonic Generation from Artificially Stacked Transition Metal Dichalcogenide Twisted Bilayers. *ACS Nano* **2014**, *8*, 2951–2958.

(69) Kresse, G.; Furthmüller, J. Efficient Iterative Schemes for Ab Initio Total-Energy Calculations Using a Plane-Wave Basis Set. *Phys. Rev. B* **1996**, *54*, 11169–11186.

(70) Kresse, G.; Joubert, D. From Ultrasoft Pseudopotentials to the Projector Augmented-Wave Method. *Phys. Rev. B* **1999**, *59*, 1758.

(71) Heyd, J.; Scuseria, G. E.; Ernzerhof, M. Hybrid Functionals Based on a Screened Coulomb Potential. *J. Chem. Phys.* **2006**, *124*, 219906.